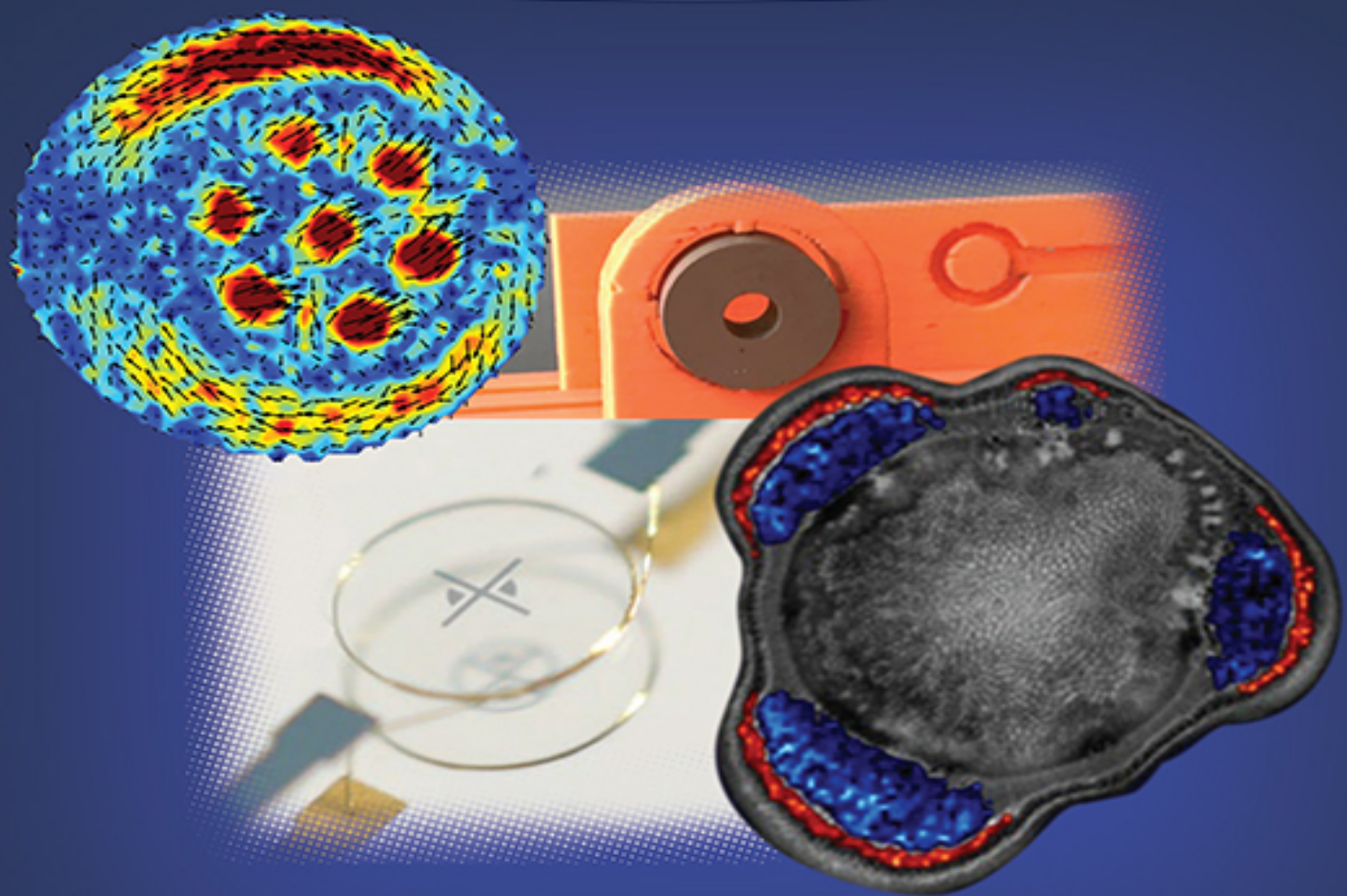


Edited by Sabina Haber-Pohlmeier, Bernhard Blümich,
and Luisa Ciobanu

Magnetic Resonance Microscopy

Instrumentation and Applications in
Engineering, Life Science, and Energy Research



Magnetic Resonance Microscopy

Instrumentation and Applications in Engineering, Life Science, and Energy Research

Edited by

*Sabina Haber-Pohlmeier
Aachen*

*Bernhard Blümich
Aachen*

*Luisa Ciobanu
Paris*

WILEY-VCH

Editors

Sabina Haber-Pohlmeier

RWTH Aachen University
Worringerweg 2
52074 Aachen
Germany

Bernhard Blümich

RWTH Aachen University
Worringerweg 2
52074 Aachen
Germany

Luisa Ciobanu

NeuroSpin, CEA-Saclay
Bat 145, Point Courier 156
91191 Gif sur Yvette France
France

Cover Image: Courtesy of Denis Wypysek, Jan Korvink, Henk Van As, and Luisa Ciobanu

All books published by WILEY-VCH are carefully produced. Nevertheless, authors, editors, and publisher do not warrant the information contained in these books, including this book, to be free of errors. Readers are advised to keep in mind that statements, data, illustrations, procedural details or other items may inadvertently be inaccurate.

Library of Congress Card No.:

Names: Haber-Pohlmeier, Sabina, 1962- editor. | Blümich, Bernhard, editor. | Ciobanu, Luisa, editor.

Title: Magnetic resonance microscopy : instrumentation and applications in engineering, life science and energy research / edited by Sabina Haber-Pohlmeier, Bernhard Blümich, Luisa Ciobanu.

Description: Hoboken, New Jersey : John Wiley & Sons, [2022] | Includes bibliographical references and index.

Identifiers: LCCN 2021061399 (print) | LCCN 2021061400 (ebook) | ISBN 9783527347605 (hardback) | ISBN 9783527827237 (pdf) | ISBN 9783527827251 (epub) | ISBN 9783527827244 (ebook)

Subjects: LCSH: Magnetic resonance microscopy. | Magnetic resonance microscopy—Industrial applications.

Classification: LCC QC762.6.M34 M344 2022 (print) | LCC QC762.6.M34 (ebook) | DDC 502.8/2--dc23/eng20220215

LC record available at <https://lccn.loc.gov/2021061399>

LC ebook record available at <https://lccn.loc.gov/2021061400>

British Library Cataloguing-in-Publication Data

A catalogue record for this book is available from the British Library.

**Bibliographic information published by the Deutsche
Nationalbibliothek**

The Deutsche Nationalbibliothek lists this publication in the Deutsche
Nationalbibliografie; detailed bibliographic data are available on the Internet at
<http://dnb.d-nb.de>.

© 2022 Wiley-VCH GmbH, Boschstraße 12, 69469
Weinheim, Germany

All rights reserved (including those of translation into other languages). No
part of this book may be reproduced in any form – by photoprinting, microfilm,
or any other means – nor transmitted or translated into a machine language
without written permission from the publishers. Registered names, trademarks,
etc. used in this book, even when not specifically marked as such, are not to be
considered unprotected by law.

Print ISBN: 978-3-527-34760-5

ePDF ISBN: 978-3-527-82723-7

ePub ISBN: 978-3-527-82725-1

oBook ISBN: 978-3-527-82724-4

Cover Design: Wiley

Typesetting: Set in 9.5/12.5pt STIXTwoText by Integra Software Services Pvt.
Ltd, Pondicherry, India

Printing and Binding: Bell & Bain

Printed on acid-free paper

Contents

[Cover](#)

[Title page](#)

[Copyright](#)

[Foreword](#)

[Preface](#)

[Part I: Developments in Hardware and Methods](#)

[1 Microengineering Improves MR Sensitivity: Neil MacKinnon, Jan G. Korvink, and Mazin Jouda](#)

[2 Ceramic Coils for MR Microscopy: Marine A.C. Moussu, Redha Abdeddaim, Stanislav Glybovski, Stefan Enoch, and Luisa Ciobanu](#)

[3 Portable Brain Scanner Technology for Use in Emergency Medicine: Lawrence L. Wald and Clarissa Z. Cooley](#)

[4 Technology for Ultrahigh Field Imaging: Kamil Uğurbil](#)

[5 Sweep Imaging with Fourier Transformation \(SWIFT\): Djaudat Idiyatullin and Michael Garwood](#)

[6 Methods Based on Solution Flow, Improved Detection, and Hyperpolarization for Enhanced Magnetic Resonance: Patrick Berthault and Gaspard Huber](#)

[7 Advances and Adventures with Mobile NMR: Bernhard Blümich, Denis Jaschtschuk, and Christian Rehorn](#)

[Part II: Applications in Chemical Engineering](#)

[8 Ultrafast MR Techniques to Image Multi-phase Flows in Pipes and Reactors: Bubble Burst](#)

Hydrodynamics Andrew J. Sederman, Andi Reci, and Lynn F. Gladden

9 Magnetic Resonance Imaging of Membrane Filtration Processes Denis Wypysek and Matthias Wessling

10 Whither NMR of Biofilms? Joseph D. Seymour, Gisela Guthausen, and Catherine M. Kirkland

11 MRI of Transport and Flow in Plants and Foods Maria Raquel Serial, Camilla Terenzi, John van Duynhoven, and Henk Van As

Part III: Applications in Life Sciences

12 MRI of Single Cells Labeled with Superparamagnetic Iron Oxide Nanoparticles: Cornelius Faber

13 Imaging Biomarkers for Alzheimer's Disease Using Magnetic Resonance Microscopy: Alexandra Badea, Jacques A. Stout, Robert J. Anderson, Gary P. Cofer, Leo L. Duan, and Joshua T. Vogelstein

14 NMR Imaging of Slow Flows in the Root-Soil Compartment: Sabina Haber-Pohlmeier, Petrik Galvosas, Jie Wang, and Andreas Pohlmeier

15 Magnetic Resonance Studies of Water in Wood Materials: Bruce J. Balcom and Minghui Zhang

Part IV: Applications in Energy Research

16 In Situ Spectroscopic Imaging of Devices for Electrochemical Storage with Focus on the Solid Components: Elodie Salager

17 Magnetic Field Map Measurements and Operando NMR/MRI as a Diagnostic Tool for the Battery Condition: Stefan Benders and Alexej Jerschow

[18 Magnetic Resonance Imaging of Sodium-Ion Batteries: Claire L. Doswell, Galina E. Pavlovskaya, Thomas Meersmann, and Melanie M. Britton](#)

[19 The Fun of Applications – a Perspective: Y.-Q. Song](#)

[Index](#)

[End User License Agreement](#)

List of Illustrations

Chapter 1

[Figure 1.1 A micro Helmholtz coil manufactured...](#)

[Figure 1.2 MR microimaging of a 154-nl deionized...](#)

[Figure 1.3 The Lenz lens \(LL\) collects the...](#)

[Figure 1.4 A comparison of the LL performance...](#)

[Figure 1.5 A Helmholtz micro coil with a wire...](#)

[Figure 1.6 Sensitivity enhancement of the micro...](#)

[Figure 1.7 Top: Magnetic resonance \(MR\) compatible...](#)

[Figure 1.8 Porosity and connectivity analysis...](#)

[Figure 1.9 Magnetic resonance \(MR\) and...](#)

[Figure 1.10 Microstructural reorganization...](#)

[Figure 1.11 Photograph of a microfluidic...](#)

[Figure 1.12 Membrane-contacting devices for...](#)

[Figure 1.13 Photograph of a fully integrated...](#)

Chapter 2

[Figure 2.1 TE₀₁₆ mode of a...](#)

[Figure 2.2 Resonant mode field...](#)

[Figure 2.3 Electromagnetic field distribution of the...](#)

[Figure 2.4 Quantification of the TE...](#)

[Figure 2.5 Schematics of the sample, typically contained in a water tube.](#)

[Figure 2.6 Example of tuning...](#)

[Figure 2.7 Signal-to-noise ratio \(SNR\) gain displayed...](#)

[Figure 2.8 Relative error between the numerical...](#)

[Figure 2.9 Comparison of the SNR predictions...](#)

[Figure 2.10 Example of excitation source: an electric...](#)

[Figure 2.11 Influence on \(left\) the reflection coefficient...](#)

[Figure 2.12 Experimental setup...](#)

[Figure 2.13 Temperature dependence of the ceramic...](#)

[Figure 2.14 Measured transmit field pattern...](#)

[Figure 2.15 Experimental comparison of the...](#)

[Figure 2.16 Coupling model of the first TE modes...](#)

[Figure 2.17 MR images of plant petioles...](#)

Chapter 3

[Figure 3.1 Superconducting MRI systems recently...](#)

[Figure 3.2 A potential portable brain magnetic...](#)

[Figure 3.3 Single-sided brain magnetic resonance...](#)

[Figure 3.4 A low-cost, lightweight...](#)

[Figure 3.5 MR devices designed to support...](#)

[Figure 3.6 Tradeoffs in superconducting solenoid...](#)

[Figure 3.7 Halbach arrays of permanent magnets...](#)

[Figure 3.8 Response of a low-field magnetic resonance...](#)

[Figure 3.9 Retrospective EMI correction of...](#)

Chapter 4

[Figure 4.1 First functional images reported...](#)

[Figure 4.2 Prediction accuracy for five models...](#)

[Figure 4.3 Functional contrast-to-noise ratio...](#)

[Figure 4.4 Noise amplification due to parallel...](#)

[Figure 4.5 Signal-to-noise ratio \(SNR\) at...](#)

[Figure 4.6 Initial images obtained from the human...](#)

Chapter 5

[Figure 5.1 Transformation of nuclear magnetic resonance excitation...](#)

[Figure 5.2 Comparison of different AM and FM...](#)

[Figure 5.3 Schematic of original SWIFT sequence. Typical...](#)

[Figure 5.4 The x, y, and z gradient...](#)

[Figure 5.5 Plot showing acoustic noise measurements during...](#)

[Figure 5.6 Two methods for reducing bullseye artifacts...](#)

[Figure 5.7 The sinograms and images before \(left...](#)

[Figure 5.8 Maximum intensity projections of SWIFT images...](#)

[Figure 5.9 Selected slices of ex vivo SWIFT...](#)

[Figure 5.10 SWIFT images \(top\) and schematic of...](#)

[Figure 5.11 Images of different spin pools and...](#)

[Figure 5.12 Gradients used for the 4D spectroscopic...](#)

[Figure 5.13 The slices of 4D spectroscopic images...](#)

[Figure 5.14 Schematic presentation of sequences \(left\) and...](#)

[Figure 5.15 3D cine magnetic resonance imaging of...](#)

[Figure 5.16 Schematics depicting pulse sequences \(on left...](#)

[Figure 5.17 The multi-band SWIFT \(MB-SWIFT...](#)

[Figure 5.18 Preoperative assessment of mandibular invasion with...](#)

[Figure 5.19 Functional response of the rat brain...](#)

[Figure 5.20 Tibia bone images with brass implant...](#)

[Figure 5.21 The schematic explains a super-resolution...](#)

[Figure 5.22 Graphical presentation of coil connection and...](#)

[Figure 5.23 Images of a human total knee...](#)

[Figure 5.24 The first in vivo human head...](#)

[Figure 5.25 Calculated radiofrequency \(RF\) amplitudes needed for...](#)

Chapter 6

[Figure 6.1 Main hyperpolarization methods. For details on...](#)

[Figure 6.2 Axial \$^1\text{H}\$ echo...](#)

[Figure 6.3 \$^{129}\text{Xe}\$ magnetic resonance...](#)

[Figure 6.4 \(a\) Principle of the \(hyper\)CEST...](#)

[Figure 6.5 3D-printed nuclear magnetic resonance inserts...](#)

[Figure 6.6 Amount of final magnetization as a...](#)

[Figure 6.7 Laser-polarized \$^{129}\text{Xe}\$...](#)

[Figure 6.8 \(a\) Principle of the device delivering...](#)

Chapter 7

[Figure 7.1 Stray-field sensors. Sweet-spot sensors...](#)

[Figure 7.2 The impact of sample misalignment with...](#)

[Figure 7.3 Tire analysis with the NMR-MOUSE...](#)

[Figure 7.4 Profiling violin backs \[21,31\]. \(a...](#)

[Figure 7.5 Study of sandstone heat damage in...](#)

[Figure 7.6 Wall paintings in the Sala del...](#)

[Figure 7.7 Frescoes and their depth profiles. \(a...](#)

[Figure 7.8 NMR depth profiling of biofilms in...](#)

Chapter 8

[Figure 8.1 \(a\) Schematic of the experimental setup...](#)

[Figure 8.2 The evolution of the map of...](#)

[Figure 8.3 The evolution of the velocity in...](#)

[Figure 8.4 The map of the out-of...](#)

[Figure 8.5 The evolution of the map of...](#)

[Figure 8.6 The map of the out-of...](#)

Chapter 9

[Figure 9.1 \(a\) Scheme of a basic membrane...](#)

[Figure 9.2 \(a\) Illustration of concentration polarization. \(b...](#)

[Figure 9.3 Flow through a hollow fiber membrane...](#)

[Figure 9.4 Chemical shift images of the oil...](#)

[Figure 9.5 Two-dimensional oil-selective cross-sectional...](#)

[Figure 9.6 \(a\) Length averaged permeate flux J...](#)

[Figure 9.7 Two-dimensional cross-sectional T...](#)

[Figure 9.8 \(a\) Growth in the thickest part...](#)

[Figure 9.9 \(a\) Local cumulative permeate flux as...](#)

[Figure 9.10 Particle deposition on structured and round...](#)

[Figure 9.11 Dead-end filtration \(a\) with Ca...](#)

[Figure 9.12 MRI images at different filtration steps...](#)

[Figure 9.13 \$T_1\$ - and T...](#)

[Figure 9.14 MRI of pure water dead-end...](#)

[Figure 9.15 Top: images showing the deposition of...](#)

[Figure 9.16 \(a.i\) to \(c.i\) Magnetic...](#)

[Figure 9.17 \(a\) Two-dimensional velocity maps above...](#)

[Figure 9.18 Cross-sectional view of the polymeric...](#)

[Figure 9.19 Flow-magnetic resonance imaging of the...](#)

[Figure 9.20 Lumen volume flow evolution measured by...](#)

[Figure 9.21 Velocity-weighted spin-density images measured...](#)

[Figure 9.22 Magnetic resonance imaging scans of central...](#)

[Figure 9.23 Cross-sectional view of the z...](#)

[Figure 9.24 Temporal evolution of cake layer formation...](#)

[Figure 9.25 The grid structure serves as a...](#)

Chapter 10

[Figure 10.1 Echo attenuation and propagator data as...](#)

[Figure 10.2 Propagators at \$\Delta = 300\$ ms as...](#)

[Figure 10.3 Magnetic resonance O...](#)

[Figure 10.4 Magnetic resonance image of a biofilm...](#)

Chapter 11

[Figure 11.1 Schematic drawing of long-distance transport...](#)

[Figure 11.2 Localized flow measurements of water and...](#)

[Figure 11.3 \$^1\text{H}\$ Rheo-MRI...](#)

[Figure 11.4 \$^1\text{H}\$ MRI velocimetry...](#)

[Figure 11.5 \$^1\text{H}\$ Rheo-MRI...](#)

Chapter 12

[Figure 12.1 Frequency distortion and resulting signal reduction...](#)

[Figure 12.2 Simulation of image contrast of a...](#)

[Figure 12.3 Magnetic resonance imaging \(MRI\) detection of...](#)

[Figure 12.4 In vivo detected cells can be...](#)

[Figure 12.5 Simulation of image contrast of a...](#)

Chapter 13

[Figure 13.1 Opening the blood-brain barrier...](#)

[Figure 13.2 Morphometric studies assess group differences, and...](#)

[Figure 13.3 The small animal multivariate brain analysis...](#)

[Figure 13.4 In vivo magnetic resonance imaging \(MRI\)...](#)

[Figure 13.5 \(A\) Ex vivo diffusion tensor imaging...](#)

[Figure 13.6 APOE4HN models of late onset Alzheimer...](#)

[Figure 13.7 Voxel-based analysis \(VBA\) evaluation. Control...](#)

[Figure 13.8 Voxel-based analysis \(VBA\) is sensitive...](#)

[Figure 13.9 A pulse sequence for diffusion-weighted...](#)

[Figure 13.10 \(A\) Fractional anisotropy \(FA\) reductions in...](#)

[Figure 13.11 Diffusion tensor imaging \(DTI\) validation with...](#)

[Figure 13.12 Fractional anisotropy \(FA\) analyses suggest vulnerable...](#)

[Figure 13.13 Mice show loss of connectivity with...](#)

[Figure 13.14 Subgraph identification based on the Wasserstein...](#)

[Figure 13.15 Simulations based on subsampling a 120...](#)

[Figure 13.16 Simulations based on a fully sampled...](#)

[Figure 13.17 To identify vulnerable networks we co...](#)

[Figure 13.18 The six largest bundles of the...](#)

[Figure 13.19 The three apolipoprotein E \(APOE\) alleles...](#)

[Figure 13.20 Predictive modeling approach in a reduced...](#)

[Figure 13.21 Using volume \(A\), manganese-enhanced magnetic...](#)

Chapter 14

[Figure 14.1 Water flow in the soil-...](#)

[Figure 14.2 Neutron radiography of water uptake in...](#)

[Figure 14.3 Determination of root water uptake rates...](#)

[Figure 14.4 MRI of a *Stachys sylvatica* stem...](#)

[Figure 14.5 Cross-sectional image of root bundles...](#)

[Figure 14.6 Flow patterns in a homogeneous sand...](#)

[Figure 14.7 Results for the heterogeneous flow phantom...](#)

[Figure 14.8 Three-dimensional flow field for the...](#)

[Figure 14.9 Modified 13-interval stimulated echo acquisition...](#)

[Figure 14.10 Test of the performance of the...](#)

[Figure 14.11 Root anatomy of Vicia faba. \(a...](#)

[Figure 14.12 Flow measurements in the root system...](#)

[Figure 14.13 Sketch of possible flow vector compositions...](#)

Chapter 15

[Figure 15.1 Cross-sectional light microscope view \(left...](#)

[Figure 15.2 Macroscopic structure of a tree in...](#)

[Figure 15.3 Plot of \$^1\text{H}\$...](#)

[Figure 15.4 Semilog plot of \$^1\$...](#)

[Figure 15.5 Schematic diagram of wood log moisture...](#)

[Figure 15.6 Total moisture content \(MC\) \(triangle\), lumen...](#)

[Figure 15.7 Local image intensity versus moisture content...](#)

[Figure 15.8 Moisture content measurement spatially resolved in...](#)

[Figure 15.9 2D slices from 3D maps of...](#)

Chapter 16

[Figure 16.1 Schematics of lithium-ion battery \(LiB...](#)

[Figure 16.2 Lithium-ion battery devices. \(a\).
Cylindrical...](#)

[Figure 16.3 General experimental setup of an in...](#)

[Figure 16.4 In situ \$^7\text{Li}\$...](#)

[Figure 16.5 Electrochemical cells for in situ
magnetic...](#)

[Figure 16.6 Chemical shift 1D imaging sequence.
A...](#)

[Figure 16.7 Chemical shift imaging of the
metallic...](#)

[Figure 16.8 Left: plot showing the time \(capacity...](#)

[Figure 16.9 \(a\) Schematic of a symmetrical Li...](#)

[Figure 16.10 Image selected in vivo spectroscopy
\(ISIS...](#)

[Figure 16.11 Schematic principle of 1D-ISIS \(one...](#)

[Figure 16.12 \$^7\text{Li}\$ scanning image...](#)

[Figure 16.13 2D X-band electron paramagnetic
resonance...](#)

Chapter 17

[Figure 17.1 Magnetic resonance imaging \(MRI\)
time series...](#)

[Figure 17.2 In situ \$^1\text{H}\$...](#)

[Figure 17.3 Left: plots of the calculated field...](#)

[Figure 17.4 Sample placement and holder in the...](#)

[Figure 17.5 \(a\) Series of magnetic field maps...](#)

[Figure 17.6 Magnetic field maps for the defective...](#)

[Figure 17.7 Left, top: \$^1\text{H}\$...](#)

[Figure 17.8 Left \(a-c\): Slices through...](#)

[Figure 17.9 Magnetic field maps and histograms during...](#)

[Figure 17.10 Longitudinal xz-slices through 3D DCF...](#)

[Figure 17.11 Relative measurements of the oscillating fields...](#)

[Figure 17.12 Experimental susceptometry setup. \(a\) Side view...](#)

[Figure 17.13 Magnetic field and corresponding...](#)

[Figure 17.14 Schematic of a pouch cell battery...](#)

[Figure 17.15 \$^7\text{Li}\$ nuclear magnetic...](#)

Chapter 18

[Figure 18.1 Three-dimensional \$^7\text{Li}\$...](#)

[Figure 18.2 3D \$^1\text{H}\$ Fast...](#)

[Figure 18.3 One-dimensional \$^{23}\text{Na}\$...](#)

[Figure 18.4 Exterior \(a\) and cutaway of the...](#)

[Figure 18.5 3D \$^1\text{H}\$ magnetic...](#)

[Figure 18.6 \$^{23}\text{Na}\$ nuclear magnetic...](#)

[Figure 18.7 2D \$^{23}\text{Na}\$ magnetic...](#)

[Figure 18.8 2D \$^{23}\text{Na}\$ magnetic...](#)

[Figure 18.9 \$^{23}\text{Na}\$ nuclear magnetic...](#)

[Figure 18.10 \$^{23}\text{Na}\$ nuclear magnetic...](#)

[Figure 18.11 2D \$^{23}\text{Na}\$ magnetic...](#)

[Figure 18.12 Images of the surface of the...](#)

[Figure 18.13 \$^{23}\text{Na}\$ nuclear magnetic...](#)

[Figure 18.14 \$^{23}\text{Na}\$ nuclear magnetic...](#)

List of Tables

Chapter 2

[Table 2.1 Literature review of dielectric probes for MRI.](#)

Chapter 4

[Table 4.1 Preliminary data on the ratio...](#)

Chapter 11

[Table 11.1 Overview of the past...](#)

[Table 11.2 Overview of the past...](#)

Chapter 12

[Table 12.1 Types of iron oxide nanoparticle by size.](#)

Foreword

This book is the fourth in the Wiley-VCH series on *Magnetic Resonance Microscopy*, a series linked in spirit to the *International Conference on Magnetic Resonance Microscopy* (ICMRM). Winfried Kuhn and Bernhard Blümich organized the first meeting of this biannual conference in 1991 in Heidelberg, which led to the first book in this series. That Heidelberg meeting is also when Paul Callaghan burst upon the scene (with his student Yang Xia, who remains active in these meetings) with his new, but now classic, book *Principles of Nuclear Magnetic Resonance Microscopy* (Oxford University Press) – what timing! The wider appearance of magnetic gradient fields in the portfolio of magnetic resonance methods for imaging and studies of molecular transport phenomena was an exciting prospect. It motivated the still ongoing ICMRM conference series and the associated books, which summarize the progress in this field with chapters written by leading experts, among them Nobel Prize awardees Paul Lauterbur and Sir Peter Mansfield as well as Sir Paul Callaghan, who shaped that community like a force of nature from then on until his untimely death in 2012. Also, our brilliant colleague Robert Blinc from Slovenia attended the first ICMRM but had to leave early following an announcement during one of the sessions effectively saying “Professor Blinc, you are needed back in your country,” at which Robert Blinc stood up and left to facilitate the independence of Slovenia from Socialist Federal Republic of Yugoslavia. We were witnessing the birth of a country, a unique experience for most of us. At the third meeting in Würzburg, the brave suggestion to hold a meeting in North America was accepted. Thus, the fourth meeting was in Albuquerque and ICMRM has now a truly international

presence, having ventured as far away as Utsunomiya and Beijing. These meetings, originally dubbed the Heidelberg Meetings, have been at the forefront of amazing developments and accompanying applications of magnetic resonance. Despite the inclusion of the word *microscopy* in their name, they represent the much broader area of magnetic resonance with spatial resolution, which is expressed by the title of the second book from the Albuquerque meeting, *Spatially Resolved Magnetic Resonance*, as well as the organizing *Division of Spatially Resolved Magnetic Resonance* of the *AMPERE Society*. Thanks to the advances over three decades, we have micrometer spatial resolution in magnetic resonance imaging today, while in the early days the word microscopy was understood as a tool to see things hard to visualize just by eye. We believe the broad range of the science and applications of magnetic resonance represented in these meetings is unique to all science and the field displays no hint of imminent stagnation – welcome news to all of us. I would like to close this Foreword with the observation that Bernhard Blümich, who with Winfried Kuhn founded these meetings 30 years ago, is still actively involved here as one of the editors of this book. I salute him for his continued contributions to the field and support of this conference.

Eiichi Fukushima
Albuquerque, 2021

Preface

Magnetic resonance microscopy (MRM) has focused on magnetic resonance imaging (MRI) applied to objects of smaller scale and higher spatial resolution for more than three decades. After the pioneering work by Eccles, Callaghan, Aguayo, Blackband, Johnson et al. in 1986, MRM quickly spread to, among other fields, chemistry, histology, and materials research. Since 1992, the edited book series *Magnetic Resonance Microscopy* has provided an important voice describing the latest developments in spatially resolved magnetic resonance methods and their applications far beyond the scope of medical diagnostics. An excellent introduction to MRM, focusing on the practical aspects of high magnetic fields and on the study of biological systems, was authored in 2017 by Luisa Ciobanu: *Microscopic Magnetic Resonance Imaging: A Practical Perspective* (Pan Stanford, Singapore, 2017). Our book complements this monograph by showing the use of MRM and related techniques in a much broader area and on a wider scale, which extends from chemical engineering to plant research and battery applications, highlighting the interdisciplinary nature of MRM.

The book opens with a section on hardware and methodology, covering aspects of micro-engineering, magnet technology, coil performance, and hyperpolarization to improve signal-to-noise ratio, a major bottleneck of MRM. Specific pulse sequences and developments in the field of mobile nuclear magnetic resonance are further topics of this first chapter. The following parts, 2 and 3, review essential processes such as filtration, multi-phase flows and transport, and a wide range of systems from biomarkers via single cells to plants

and biofilms. Part 4 focuses on energy research, which is becoming increasingly important due to the globally growing environmental problems. It reports on battery types and their developments and how battery states can be recorded and characterized with MRM. However, we would like to point out that only a small number of applications could be addressed in this book. Finally, the last chapter advocates that theory and applications should not be treated separately, because much can be gained from their complementarity.

The main aim of this book is to convince aspiring and established scientists from all fields that MRM is a versatile nuclear magnetic resonance (NMR) method that is capable of answering many questions from both the laboratory and everyday life. The book seeks to inspire a new readership from industries and innovative research directions to create synergies by adding MRM to their expertise.

The editors thank all the authors for contributing their invaluable knowledge to this book during a time challenged by COVID-19. Our thanks also go to the kind staff of the Wiley books department, who helped us with advice and support throughout the whole editing process.

Sabina Haber-Pohlmeier
Luisa Ciobanu
Bernhard Blümich
Summer 2021

Part I

Developments in Hardware and Methods

1

Microengineering Improves MR Sensitivity

Neil MacKinnon, Jan G. Korvink, and Mazin Jouda

Institute of Microstructure Technology, Karlsruhe Institute of Technology, Eggenstein-Leopoldshafen, Germany

1.1 Introduction

Thirty years have passed since 1991 when Paul Callaghan published his book on magnetic resonance microscopy [[1](#)], and many works have subsequently appeared that have made numerous advances in this exciting field possible. Our goal for this chapter is to (informally) revisit some of Callaghan's analysis, to reflect on it, and then take account of some of the advances and insights that have been reported since then.

1.1.1 Comparative Electromagnetic Radiation Imaging

Paul Callaghan's book [[1](#)] is perhaps the first publication to consider magnetic resonance imaging (MRI) in the same light as optical microscopy. This will also be our starting point.

Until the advent of super-resolution microscopy, refractive optical microscopy was essentially a radiation scattering method, in which a beam of photons from an independent light source was sent on its way to scatter off objects, followed by traversal of the beam through a focusing objective on its way back to a detector, to thereby reveal the structure and composition of the scattering object. The

limitations of this approach, in terms of resolution, is known as the Abbe limit $\delta = \lambda / (2 n \sin \theta)$, where n is the refractive index, θ the half-angle of the spot subtended by the lens, and λ the radiation wavelength.

Using radio waves taken for convenience at 300 MHz, a thus interpreted refractive MRI system would have a resolution of ~ 500 mm, which is a dire prospect for applications of MRI. In a seminal paper, Mansfield et al. [2] reported on a form of nuclear magnetic resonance (NMR) diffraction, in which they considered a solid-state periodic lattice of spins in a macroscopically sized lattice, revealing diffraction patterns on the order of the lattice. As a follow-up to this idea, Blümmler et al. [3] and Bernhard Blümich [4] reported (the latter in a paper dedicated to Paul Callaghan) on an interesting intertwining of concepts of the \mathbf{k} -space vector of refractive MRI and the spatial periodicity of a lattice-like diffractive structure, further exploring diffractive imaging. Blümich's paper contains a few more gems worth discussing, but would distract us too far from the optical viewpoint we are considering here.

Near-field effects can be further exploited to increase the resolution of an imaging system. At optical wavelengths, one is hardly able to extend beyond 200 nm of resolution with currently available light sources. "The diffraction limit of light is 100 times the size of structures that cell biologists study as they characterise events in organelles or membranes," Hari Schroff (NIH/NIBIB) is quoted to say in [5], yet below 200 nm "is where most cellular action is," the author notes. The alternative is to avoid scattering as an imaging paradigm, instead, to image photon sources (also known as quantum emitters).

Interestingly, deep space astronomy always worked this way around by observing photon emitters, so that astronomers only consider objects that were once

themselves sources of radiation, such as stars and their predecessors and descendants. In astronomy, the limit of resolution is therefore not dominated by the wavelength of the radiation, which can be very small when compared to the size and distance of the astronomical objects, but rather by the measuring instrument's principle of operation, its detection sensitivity, and in particular, its effective aperture.

When imaging radiation sources, such as single photon emitters in molecules, we now know that we can greatly improve on the Abbe limit, by about a factor of 10, especially when combined with techniques of stimulated emission and depletion, and one of the numerous variations based on fluorophore emission dynamics. These techniques, which have revolutionized cellular biology and won its inventor Stefan Hell the Nobel Prize in 2014, are of course not accessible to astronomers, who would have to wait too long for excitation signals to pass from observer to object and back again. But for cell biology this is not problematic. Although at currently ~ 30 nm, the resolution is still far from the desired 1 nm limit, advances in image processing present a feasible route to achieve further improvements. But the technique also raises some questions. Sample preparation is very difficult, and imaging is indirect as fluorophores have to be invasively attached to interesting molecules, almost certainly modifying their behavior.

Magnetic resonance microimaging is a noninvasive technique that is clearly more closely related to stimulated emission depletion (STED) microscopy than to conventional scattering light microscopy. A localized atomic nucleus' spin is a quantum absorber/emitter. By localizing the excitation field spatially or by frequency, a sub-selection of the spins in a sample can be prepared to absorb radiation. Further localization can ensure that emission of radiation energy is again sub-selected, for example along the

geometrical intersection of two orthogonal manifold slices, the one for excitation, the other for emission. A range of further techniques, such as available through relaxation contrast, or phase accumulation, can again further sub-select spins before readout, thereby improving resolution in direct analogy to the techniques of fluorophore emission dynamics. Noninvasive Faraday-detected MRI has been reported down to $\sim 3 \mu\text{m}$ resolution [6], which is already five orders of magnitude below the radiation wavelength. Nevertheless, even though MRI records radio frequency emissions, this is done almost exclusively through near-field interactions, i.e. by Faraday induction, and not from a beam or ray that requires a lens for focusing.

One of the limitations in NMR is certainly that a single quantum emission event is not yet readily observable as it would be in photonics, even though Dan Rugar showed that a single spin can be observed [7]. Thus all Faraday induction-acquired MRI images have to resort to averaging of a vast number of emission events, and over extended time, to yield useful information. If detection sensitivity were to be increased, fewer emitters could be used, and could perhaps be averaged over shorter times.

1.1.2 Limit of Detection

The statistical polarization level, i.e. that proportion of the total spin population that is available for quantum emission, is an additional cause of lack of signal. Proton spins for example are indistinguishable fermions, with a level occupation that follows

$$\langle N_i \rangle = \frac{1}{e^{(\epsilon_i - \mu)/kT} \pm 1} \quad (1.1)$$

and which collapses to Maxwell-Boltzmann statistics when $e^{(\epsilon_i - \mu)/kT} \gg 1$, because the energy of a proton flip $\gamma \hbar B_0 =$

3.3×10^{-25} J is tiny compared with the thermal energy $kT = 4.11 \times 10^{-21}$ J. Thus at typical equilibrium polarization levels at 11.7 T, a factor of only 10^{-4} in excess in population difference with respect to the Fermi level μ can contribute to the signal. An imaging voxel size is therefore principally limited by polarization, because we find – for microcoils at their limit of detection – a sample containing around 10^{13} spins is needed to form an observable signal. Clearly, this sets a lower concentration limit once the voxel size is specified. For example, at the average size of a single eukaryotic cell of $(10 \mu\text{m})^3$, containing the required nuclei, implies a concentration of at least 1.66 μM . By increasing polarization, the voxel size is thus principally reduced, or the lower concentration limit is reduced, which could be achieved by resorting to out-of-equilibrium polarization techniques such as parahydrogen-induced polarization (PHiP), signal amplification by reversible exchange (SABRE), or dynamic nuclear polarization (DNP), all of which are rather hard to perform noninvasively, and hard to selectively localize too. We will return to this point shortly. One of the key advantages of MR-based microscopy is the ability to noninvasively reveal molecular composition, correlated with morphology. From the perspective of biological systems, this can be leveraged to monitor, for example, spatially resolved metabolism. To estimate the best achievable spatial resolution (voxel size), signal-to-noise ratio (SNR) should be considered in the context of the metabolically active system. Key parameters are the molecule abundances (concentrations) and timescale that are targeted. Consider a spatially resolved fluxomic investigation: can one estimate a realistic MRI spatial resolution taking into consideration the expected biological dynamics? Alternatively, what is the smallest biological structure with which metabolic flux can be measured –

thus, is it possible to monitor flux at the level of an organelle, single cell, cell cluster, or tissue?

Water is the most abundant molecule in biosystems and can be used as a useful reference from which scaling based on metabolite concentrations can be made. Using only the physical volume of a water molecule (0.03 nm^3), and an optimistic limit of detection (LOD) of 10^{13} spins, then an order of magnitude estimate of the smallest voxel is 0.1 pl (approximately $4.5 \text{ }\mu\text{m}$ isotropic resolution). This is approximately the volume of a single red blood cell. Intracellular metabolite concentrations vary over several orders of magnitude, with the most abundant molecules typically in the tens of millimolar regime. The best-case scenario scaling factor is then 10^4 relative to water (assuming $[\text{water}] = 55 \text{ M}$), and thus the smallest voxel volume increases to 1000 pl ($100 \text{ }\mu\text{m}$ isotropic resolution). For reference, this would correspond to 10 000 red blood cells or 2 fat cells (volume 600 pl per cell). Can the resolution be improved by signal averaging as a means to enhance SNR? Assuming metabolism is active during the measurement then one must consider the turnover rate of the target metabolite(s) relative to the time over which signal averaging is performed. Enzyme catalytic (second-order) rate constants span several orders of magnitude ($k_{\text{cat}}/K_{\text{M}} \sim 10^1\text{--}10^9 \text{ s}^{-1} \text{ M}^{-1}$), with a median of $\sim 10^5 \text{ s}^{-1} \text{ M}^{-1}$ [8]. If the metabolite concentration is 100 mM , then the metabolite will encounter the “median enzyme” with a rate of 10^4 s^{-1} . At this concentration and a volume of 1000 pl , the metabolite concentration would drop below the LOD ($\sim 10 \text{ mM}$) in 6000 days giving more than sufficient time for signal averaging. At the diffusion limit $10^9 \text{ s}^{-1} \text{ M}^{-1}$ then, 6 days are required before the signal is not observable. This rough estimate takes many liberties in the assumptions (catabolic and anabolic reactions, multiple pathways,